Materials Characterization 224 (2025) 114956

Contents lists available at ScienceDirect

Materials Characterization

journal homepage: www.elsevier.com/locate/matchar

Simultaneous improvement of mechanical strength and electrical conductivity in Al-2.5 wt% Fe alloy rods with high thermal stability by high-pressure torsion extrusion

Rui Xu [a,b,c], Yemao Lu [a,c,d,*], Yuting Dai [a,b,c], Rafaela Debastiani [a,c], Horst Hahn [a,b,e], Yulia Ivanisenko [a]

[a] Institute of Nanotechnology (INT), Karlsruhe Institute of Technology (KIT), Kaiserstr. 12, 76131 Karlsruhe, Germany
[b] Joint Research Laboratory Nanomaterials, Technical University of Darmstadt (TUDa), 64287 Darmstadt, Germany
[c] Karlsruhe Nano Micro Facility (KNMFi), Karlsruhe Institute of Technology (KIT), 76344 Eggenstein-Leopoldshafen, Germany
[d] Nano and Heterogeneous Materials Center, School of Materials Science and Engineering, Nanjing University of Science and Technology, Nanjing 210094, China
[e] Aerospace and Mechanical Engineering, The University of Oklahoma, Norman 73019, United States

ARTICLE INFO

Keywords:
Heat resistant Al-alloys
High-pressure torsion extrusion
Strength
Electrical conductivity
NanoCT

ABSTRACT

The high-pressure torsion extrusion (HPTE), a severe plastic deformation (SPD) method, was applied to process rods of as-cast Al-2.5 wt% Fe alloy (Al-2.5 Fe). This technique effectively overcomes the typical trade-off between mechanical strength and electrical conductivity (EC) commonly observed in Al-alloys. Through the HPTE process, the yield strength increased from 110 MPa to 268 MPa, while the EC increased from 37.3 % IACS to 44.7 % IACS. Furthermore, the ultrafine-grained structure of the HPTE-processed Al-2.5 Fe exhibits remarkable thermal stability, maintaining its strength following annealing for 1 h at 230 °C. The effects of the HPTE-induced deformation and subsequent annealing on the microstructure were thoroughly studied using automated crystal orientation mapping (ACOM), STEM-EDX, and X-ray tomography (NanoCT). In terms of the Al matrix, grain refinement resulted in grains with an average size of 300 nm. Additionally, the previously continuous $Al_{13}Fe_4$ phase network fragmented into micrometer- and nanometer-sized particles. A theoretical analysis has shown a correlation between microstructural characteristics, mechanical strength, and EC, identifying the mechanisms responsible for the strengthening effect and the changes in EC. It indicates that the size, shape, and spatial distribution of the $Al_{13}Fe_4$ phase are crucial in determining mechanical performance, as well as affecting the thermal stability and EC of Al-2.5 Fe.

1. Introduction

As renewable energy technologies continue to advance, the electric power and automotive industries are increasingly demanding lightweight materials that combine enhanced strength, excellent thermal stability, and superior electrical conductivity. [1,2]. Al-Mg-Si alloys, such as the commercial AA6101 and AA6201, are widely used in overhead transmission lines due to their excellent balance of strength and electrical conductivity compared to other Al alloys [3,4]. However, their service temperature is limited to 90 °C, as phase transformations and the coarsening of second-phase precipitates at higher temperatures can significantly degrade their mechanical strength [3,5]. Recently, Al-based immiscible alloy systems, including Al—Fe, Al—Zr, and Al-RE alloys (RE representing rare earth elements), are drawing significant attention due to their excellent heat resistance, high electrical conductivity, and remarkable formability [6–11]. Among these, Al—Fe alloys are particularly attractive. One key reason is that Fe is a more affordable alloying element compared to Zr and RE elements. Additionally, Fe-rich intermetallic compounds, such as $Al_{13}Fe_4$ and Al_6Fe, exhibit notable thermal stability in Al—Fe alloys, primarily due to the low diffusivity of iron in aluminum [12,13]. This makes Al—Fe alloys highly suitable to elevated-temperature applications, where an increased volume fraction of thermally resistant nanoscale particles effectively inhibits grain growth through the Zener pinning mechanism [7,14]. However, as-cast Al—Fe alloys commonly have a low yield strength by virtue of the coarse grain size of Al matrix and large intermetallic particles. For example, the

* Corresponding author at: Institute of Nanotechnology (INT), Karlsruhe Institute of Technology (KIT), Kaiserstr. 12, 76131 Karlsruhe, Germany.
E-mail address: yemao.lu@kit.edu (Y. Lu).

https://doi.org/10.1016/j.matchar.2025.114956
Received 19 November 2024; Received in revised form 14 February 2025; Accepted 22 March 2025
Available online 28 March 2025

tensile strength of as-cast Al-2 wt% Fe is approximately 120 MPa [15].

Severe plastic deformation (SPD) methods, such as high-pressure torsion (HPT) and equal-channel angular pressing (ECAP), are pervasively applied to enhance the mechanical performances of aluminum alloys [16]. The aforementioned methods are effective in refining coarse-grained microstructures to the sub-micrometer level, leading to significantly improved strength in light of the Hall-Petch correlation [17]. Duchaussoy et al. [7] demonstrated that HPT deformation can simultaneously refine the Al-matrix grain size and the Fe-rich intermetallic phases to the nanoscale range in Al-2.5 Fe, significantly improving its mechanical and thermal resistance properties. However, several key challenges limit the broader commercial application of traditional SPD techniques for structural materials [18]: (i) the limited size of samples, (ii) the inability to continuously process materials, and (iii) the need for multiple deformation passes with interruptions. Furthermore, annealing treatments are often required after traditional SPD techniques to balance electrical conductivity and mechanical strength, which increases both processing time and energy consumption. For example, after HPT deformation, the yield strength of the Al-5.4 wt% Ce-3.1 wt% La alloy increased from 73 MPa to 475 MPa, while its conductivity declined from 49.5 % IACS to 39.7 % IACS. After annealing for 1 h at 280 °C, the conductivity improved to 44.7 % IACS, although it remained lower than that of the as-cast alloy [5].

High-Pressure Torsion Extrusion (HPTE) is an innovative SPD procedure capable of introducing substantial shear strain in rod-like samples within a single processing pass [19–23]. The Conform™ technique integrated with HPTE can produce rods or wires with unlimited length [24]. Omranpour et al. [21] reported that HPTE can achieve an ultrafine-grained (UFG) microstructure in pure Al rods. As demonstrated by Nugmanov et al. [22], the HPTE can increase the mechanical strength of commercially pure copper from 130 MPa to 370 MPa. Our previous studies demonstrated an increase in the mechanical strength of as-cast Al-RE alloy between 127 MPa and 225 MPa, along with an improvement in the conductivity between 54.7 % IACS and 55.7 % IACS after the HPTE deformation [23].

Our research revealed that HPTE was applied to as-cast Al-2.5 Fe alloy rods to simultaneously improve electrical conductivity and mechanical performances. Additionally, the thermal stability of the HPTE-treated Al-2.5 Fe alloy rods was also investigated. Finally, the effect of microstructural changes on concurrent improvement of mechanical performances and EC were systemically constructed to further understand this phenomenon. This research introduces an innovative strategy for developing Al alloys combining high strength, thermal stability, and excellent EC.

2. Materials and methods

In this study, an Al-2.5 wt% Fe alloy with an impurity content of less than 0.05 wt%, produced by electromagnetic casting and obtained from a commercial supplier, was used. Al-2.5 Fe alloy rods in the as-cast state, with a length of 35 mm and a diameter of 12 mm, were processed using the High-Pressure Torsion Extrusion (HPTE). Such a technique was executed at room temperature (RT) on a specially designed, computer-controlled HPTE machine (W. Klement GmbH, Lang, Austria) featuring speciel hexagonal dies (Fig. 1b). During the procedure, a translational rate was set to 2 mm/min with a rotational rate set to $\omega = 1$ rpm. Molybdenum Disulfide (MoS_2) served as one lubricator in all experiments, facilitating the extrusion process. Specifications for HPTE devices applied to our research are detailed in Ref. [19], with a description of the HPTE die in Fig. 1(a). During extrusion, each sample passed individually through the die, driven by a punch advancing at an extruding rate υ, while the lower die revolving at ω. This process subjected the material to a combination of expansion-extrusion and torsional deformation within the confined area in which the dies intersected. With respect to a single pass, the equal strain was computed through the following formula [19]:

$$\varepsilon_{HPTE} = 2\,In\frac{D1}{D0} + 2\,In\frac{D1}{D2} + \frac{2\pi\omega RD1}{\sqrt{3}\upsilon D2} \quad (1)$$

In this equation, D2, D1, and D0 act as constants with values of 10.6 mm, 14 mm, and 12 mm, separately, while R denotes the distance from the center of sample cross-section. The calculated equivalent strain values for HPTE are provided in Table 1.

After the HPTE process, the samples were annealed from 330 °C down to 80 °C. Annealing was carried out within one resistance-heat stove.

The Vickers microhardness of the samples was evaluated through a tester (Buehler Micromet). A constant load of 100 g was applied uniformly across all samples, with each indentation held for a dwell time of 15 s. Indentations were made at multiple locations on the sample cross-section, showing each indentation positioned equidistantly from its neighboring points. Tensile tests were implemented at room temperature (RT) using an initial strain rate of 10^{-3} s^{-1} using a test machine (Zwick Z100) with dog-bone samples showing a gauge length of 15 mm and a diameter of 6.85 mm, as indicated in Fig. 2. Electrical conductivity (EC, MS/m) was measured for the longitudinal and transverse cross-sections at ambient conditions through an eddy current conductivity tester (Sigmascope SMP-350, Helmut Fischer GmbH, Sindelfingen, Germany). The device was calibrated prior to each set of measurements using reference materials, ensuring an accuracy of ±0.3 %. Measurements were taken at room temperature, with samples maintained at a stable temperature for a minimum of 5 h. The samples were polished mechanically to obtain mirror-like surfaces. It was established that the

Table 1
Equivalent strain at HPTE in different sample locations was calculated using Eq. (1).

Distance from the sample center R (mm)	0	1	2	3	4
Equivalent strain at HPTE	0.9	3.3	5.7	8.1	10.5

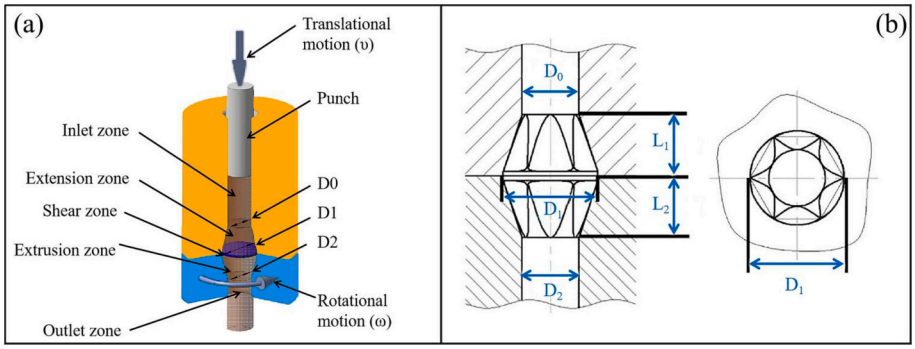

Fig. 1. Representation of the HPTE technique and its parameters (a). Detailed drawing of the HPTE die (b) (Ref. [23]).

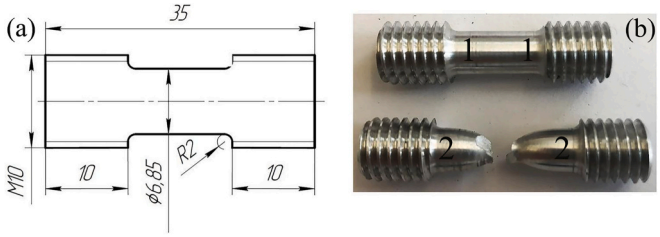

Fig. 2. (a) Schematic diagram and (b) photograph of the tensile test specimen, with dimensions in millimeters. In (b), 1 represents the specimen before the tensile test, while 2 represents the specimen after the tensile test, showing deformation and fracture characteristics.

electrical conductivity values of the longitudinal and transverse sections were nearly the same. The equation applied to denote the EC with regard to the International Annealed Copper Standard (IACS) units is below: IACS = (EC_{Al} / EC_{Cu} * 100) %, where EC_{Al} represents the alloy's conductivity in MS/m; besides, EC_{Cu} denotes the copper conductivity (58.0 MS/m). The correlation between the EC in % IACS and electrical resistivity (ER, μΩ.cm) is capable of being figured out through the formula: $K_{\%IACS} = 172.41/\rho$ [6].

In terms of the as-cast, HPTE-treated and annealed samples, crystal structure was investigated using X-ray diffraction (XRD) analysis using the Empyrean X-ray diffractometer (Malvern Panalytical, Netherlands), along with the CuKα radiation (λ = 0.15418 nm) at 40 kV and 40 mA, with a step size of 0.0167°. The XRD data was analyzed via the Rietveld refinement using HighScoreplus software to measure the Al matrix's lattice parameter (a), the lattice microstrain ($<\varepsilon^2>^{1/2}$), and the coherent scattering domain size (CSDS). To account for the instrumental contribution to XRD peak broadening, a LaB6 standard sample was used. The density (ρ) of dislocation was figured out through the formula below [17]:

$$\rho_{\perp} = 2\sqrt{3} < \varepsilon^2 >^{\frac{1}{2}} \Big/ (D \times b) \quad (2)$$

here, $b = a^*\sqrt{2}/2$ is the Burgers vector, $<\varepsilon^2>^{1/2}$ denotes the lattice microstrain, and D denotes the coherent scattering domain size.

The second phase morphology and the element distribution in the as-cast, HPTE-treated and annealed samples were explored with a Zeiss Auriga 60 scanning electron microscope (SEM) set to 20 kV. As well as an energy-dispersive X-ray spectroscopy (EDX), a backscattered electron detector (BSE) was adopted. SEM analyses were performed at three distinct locations on the transverse section of the samples: the center, the mid-radius area (approximately 2 mm from the center axis), and near the edge (approximately 4 mm from the center axis).

The Al-matrix microstructure in the mid-radius area of the as-cast, HPTE-treated, and annealed samples was further investigated through the electron backscatter diffraction (EBSD) on a Zeiss Auriga 60. Owing to the small grain size of the Al matrix and its interplay with fine second-phase particles near the edges of the HPTE-treated and annealed samples, it was challenging to make grain size measurements reliable through EBSD. Therefore, automated crystal orientation mapping (ACOM) [Ref.] was employed to investigate the microstructure in these regions. The ACOM analysis was conducted at 300 kV using a ThermoFisher Scientific Themis 300 transmission electron microscope (TEM) equipped with a NanoMegas ASTAR system for orientation map acquisition. ACOM measurements were performed with the probe size of 1.5 nm, the step size of 5 nm, with a convergence angle of 30 mrad. The TEM was operated in a microprobe mode, with a spot size of 7, a gun lens setting of 6, and a 50 μm condenser aperture 2 (C2). The convergence angle was primarily controlled by adjusting the C2 aperture. Diffraction patterns were acquired with a camera length of 245 mm. To ensure data reliability, grains with less than four pixels were eliminated automatically through the grain-dilation cleanup and adjoining orientation relationship functions via the OIM software. Using a misorientation cut-off of 2°, noise-induced erroneous orientations were adopted, while the low-angle boundaries (LAGBs) were differentiated from high-angle boundaries (HAGBs) through a misorientation cut-off of 15°. The grain size was measured using the equivalent diameter approach, with twin boundaries excluded from the calculation. In this analysis, merely grains delineated with HAGBs and consisting of at least five pixels were included. Over 500 grains were analyzed per sample. For EBSD, TEM and ACOM analysis, the samples were prepared using a conventional electro-polishing procedure with a Tenupol twinjet polisher, utilizing the standard Struers solution for aluminum. To further improve surface quality and minimize residual deformation, the samples were additionally cleaned using ion milling (Gatan, PIPS II).

Among HPTE-treated and annealed samples, the dislocation distribution and nanoscale intermetallic particles were further investigated through the TEM and scanning TEM (STEM), using a ThermoFisher Scientific Themis Z microscope. These analyses were executed on transverse sections near the sample edges. Importantly, sample preparation followed a similar process as that used for EBSD samples.

The 3D microstructure of as-cast and HPTE-treated samples was analyzed using X-ray computed tomography (nanoCT). Scanning was implemented through an Ultra X-ray microscope (Zeiss Xradia 810), which employs a chromium anode to generate a quasi-monochromatic X-ray beam with an energy of 5.4 keV. Using absorption and Zernike phase contrast mode, the system provides resolutions of 50 nm or 150 nm within fields of view of 16 μm or 65 μm, respectively. Samples measuring 6 μm × 6 μm × 10 μm were prepared via a focused ion beam and attached to a needle for scanning. Each sample underwent a 180° rotation showing an exposure time of 120 s for each projection, in Zernike phase contrast mode. The as-cast sample was scanned in a 65 μm field vision showing a pixel size of 63.6 nm, acquiring 301 projections, while the HPTE-treated sample was scanned within a 16 μm field of vision with a pixel size of 32.4 nm, acquiring 701 projections. With a filtered back projection algorithm, reconstructions were performed through Zeiss Scout and Scan Reconstructor version 13. 3D images were processed using Dragonfly ORS software [25].

3. Results

3.1. Mechanical properties, thermal stability, and electrical conductivity of the Al-2.5 Fe alloy following HPTE processing

Fig. 3a shows the microhardness values for as-cast, HPTE-treated and annealed samples. The microhardness of as-cast alloy was determined at 55 HV. Among the HPTE-treated samples, the microhardness ranged from 69 HV to 96 HV across the radius of transverse cross-sections (Fig. 3a). This hardness level remains consistent following annealing at temperatures between 80 °C and 230 °C (Fig. 3a). As the annealing temperature rose, the microhardness progressively declined to 79 HV at 280 °C as well as 73 HV at 330 °C, measured at 4 mm from the disc center. Such hardness values still exceed those of the as-cast alloy (Fig. 3a).

Fig. 3b shows the engineering stress-strain curves for the as-cast, HPTE-treated and annealed samples. The HPTE process brought about a significant rise in the mechanical strength from the initial as-cast 110 ± 3 MPa to 268 ± 5 MPa. As the annealing temperature rose to 280 °C, the mechanical strength declined to 190 ± 3 MPa, following the same trend observed in the microhardness results.

Fig. 3c reveals that the EC of the as-cast alloy reaches 37.3 ± 0.1 % IACS, but it rises to 44.7 ± 0.1 % IACS after the HPTE processing. The HPTE-treated samples exhibit a stable EC across the annealing temperature range from 80 °C to 230 °C (Fig. 3c). As annealing temperature further increases, the EC shows a mild uptick, achieving 46.6 ± 0.2 % IACS at 280 °C as well as 47.6 ± 0.2 % IACS at 330 °C.

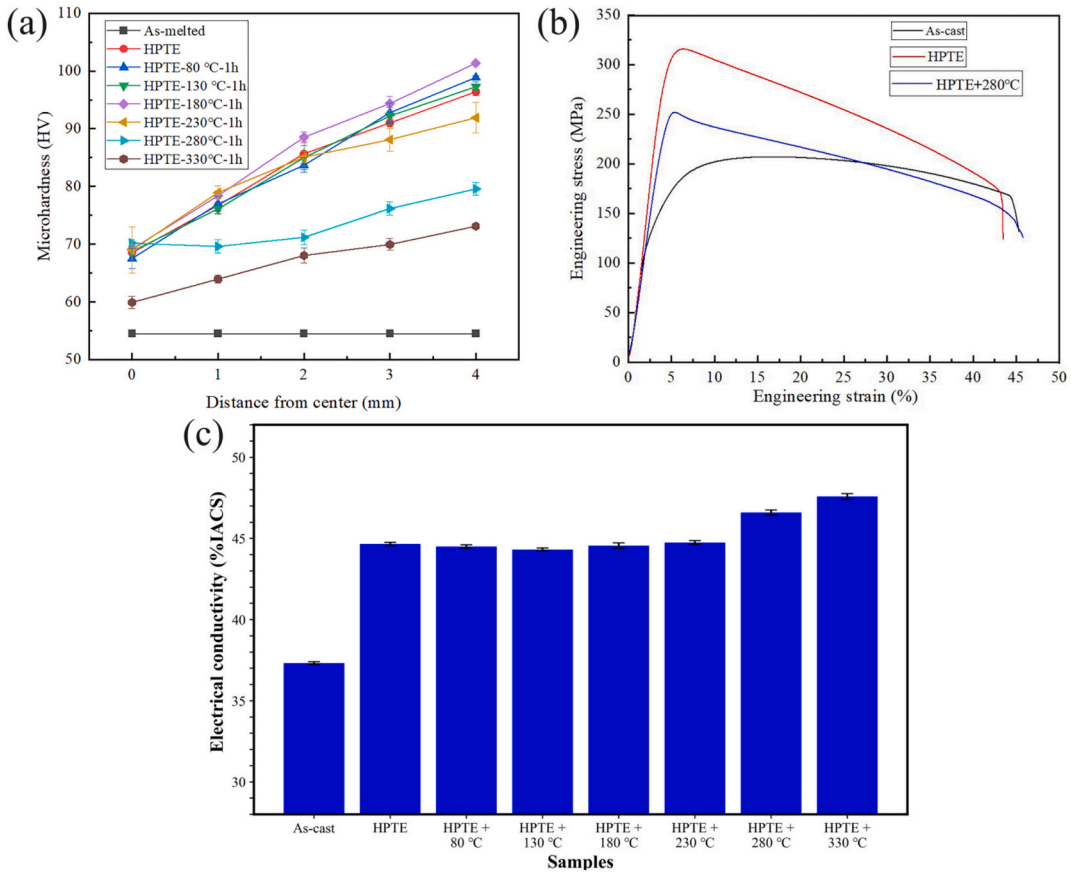

Fig. 3. Vickers microhardness at varying distances from the center (a), Engineering stress-strain curves for the as-cast alloy, the HPTE-treated sample, and the HPTE-treated and annealed sample at 280 °C (b), and the EC (% IACS) of different samples (c).

3.2. Microstructure observations

3.2.1. Microstructure of the as-cast samples

Fig. 4(a) displays the representation of the as-cast Al-2.5 Fe microstructure observed by SEM. The hypereutectic structure includes an Al matrix showing the Al—Fe intermetallic phase inclusions constituting a continuous network. Moreover, the inset highlights the lamellar structure of such intermetallic phase.

The EDX results indicate that Fe atoms are concentrated within the intermetallic particles, with no detectable Fe presence in the Al matrix (Fig. 4(b)). As expected, the results emerged given the negligible solubility of iron in aluminum at RT [26]. The dark-field TEM representation (Fig. 4(c)) manifests that the average lamella thickness of the Al—Fe intermetallic phase is 89 ± 29 nm. The inset of Fig. 4(c) displays that the corresponding SAED pattern is consistent with the $Al_{13}Fe_4$ phase in the [11 10–5] zone axis.

Fig. 5(a) presents the NanoCT image of the microstructure of the as-cast Al-2.5 Fe alloy. The 3D reconstruction reveals that the $Al_{13}Fe_4$ phase forms a continuous network-like constitution within the aluminum matrix. Fig. 5(b) displays the EBSD orientation map of the as-cast sample microstructure. The Al matrix possessed a mean grain size over 300 μm, notably exceeding the cell size of the $Al_{13}Fe_4$ phase network. Consequently, the continuous $Al_{13}Fe_4$ phase network emerges within the grains of the Al matrix.

3.2.2. Microstructural analysis of the HPTE-treated samples

Fig. 6(a-c) displays BSE-SEM representations of the HPTE-treated sample microstructure. Within regions near the rod axis, with an effective strain of about 0.9, the $Al_{13}Fe_4$ phase retains a continuous network structure, similar to that in the as-cast sample (Fig. 4(a)). At the radius midpoint, with an effective strain of around 5.7, the continuous $Al_{13}Fe_4$ network is fragmented into micrometer- and nanometer-sized particles (Fig. 6(b)). With an effective strain of 10.5 at the rod's edge, the size of particles decreases further (Fig. 6(c)). Fig. 6(d) displays a NanoCT image of the HPTE-treated Al-2.5 Fe alloy taken from the radius midpoint. The 3D reconstruction demonstrates that micrometer- and nanometer-sized particles are distributed nearly homogeneously within the aluminum matrix.

Fig. 7(a) illustrates the EBSD orientation maps of the HPTE-treated Al-2.5 Fe sample within the normal cross-section near the mid-radius. A mean grain size of the Al matrix in this HPTE-treated sample possesses is 0.57 ± 0.22 μm (Fig. 7(b)). High-angle grain boundaries (HAGBs) constitute almost 80 % (Fig. 7(c)). Fig. 7(d) displays the ACOM TEM orientation map of the HPTE-treated sample near the edge. In this region, elongated grains having a mean length of 0.51 ± 0.14 μm and width of 0.11 ± 0.05 μm are examined. The mean grain size reaches 0.29 ± 0.14 μm (Fig. 7(e)). The elongation of the grains is likely a result of the HPTE deformation component, caused by friction between the rod sample and the HPTE die walls [19,22]. Similar grain elongation in the edge region has been reported following HPTE processing of pure Al [21] and Al 6101 alloy [27]. There is a tendency for the fraction of HAGBs to increase from 79 % to 83 % (Fig. 7(c), (f)). These findings suggest that HPTE processing at RT can induce an UFG microstructure in Al-2.5 Fe alloy, in agreement with microhardness measurements (Fig. 3(a)).

Noticeably, the grain size of the as-cast Al—Fe alloy can be refined to approximately 300 nm, which is smaller than that achieved for pure Al subjected to HPTE under similar conditions [21]. The secondary-phase particles are capable of effectively pinning dislocations generated during deformation, resulting in their accumulation in deformation zones within the alloy matrix, which leads to obvious local dislocation gradients [28–32]. In such areas, novel high-angle borders can form at

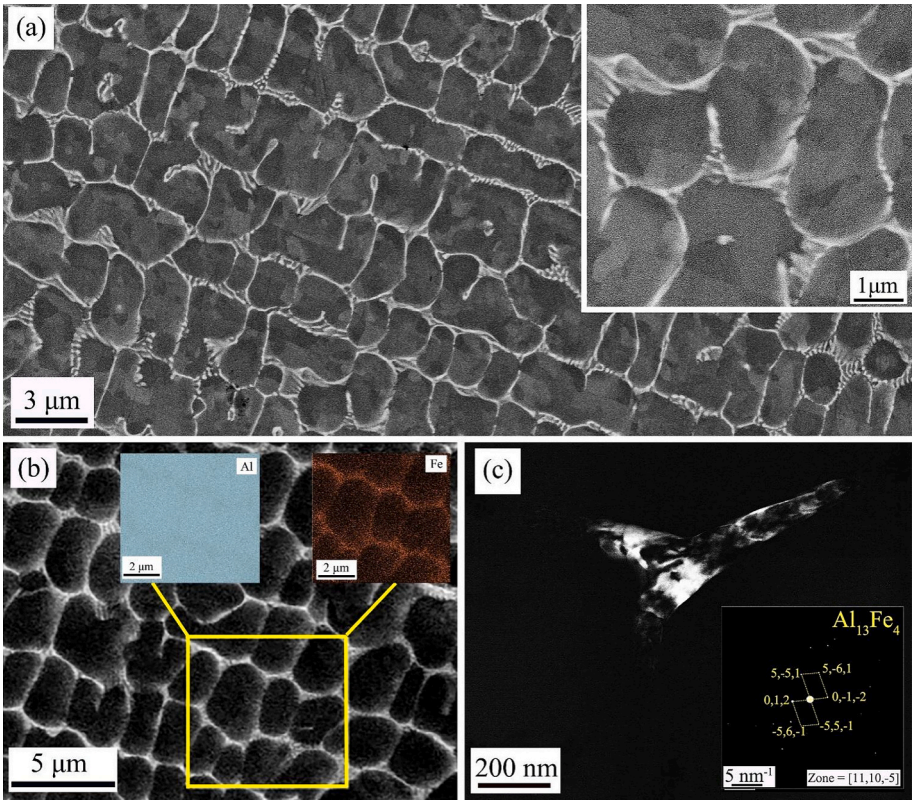

Fig. 4. (a) the SEM representation of the hypereutectic microstructure in the as-cast alloy, with an inset exhibiting the elevated magnification of the Al-2.5 Fe intermetallic phase morphology; (b) The EDX results of as-cast samples; (c) dark-field TEM image of the $Al_{13}Fe_4$ phase.

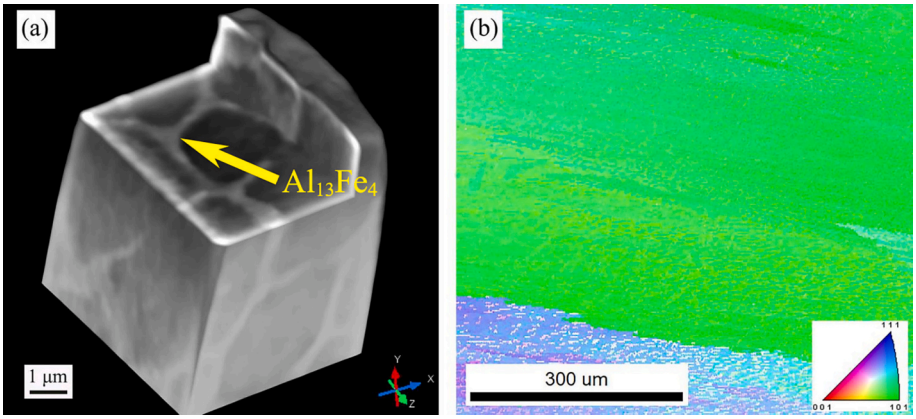

Fig. 5. (a) NanoCT representation of the as-cast Al—Fe alloy; (b) EBSD orientation map.

comparatively low strain levels [28–30].

Fig. 8(a-b) displays STEM-EDX images showing the microstructure of the HPTE-treated sample at edge positions along the rod's normal cross-section, where the equivalent strain is 10.5. Nanoscale $Al_{13}Fe_4$ phase particles are distributed along the GBs and within the Al grains (Fig. 8 (a)). It is evident that these nanoparticles act as pinning sites for dislocations within the Al grains (Fig. 8(a)). EDX analysis confirms that Fe atoms are confined to the intermetallic particles and are not detected within the Al matrix (Fig. 8(b)).

3.2.3. *Microstructural analysis of the HPTE-treated and annealed samples*

Fig. 9(a-c) unveils EBSD orientation maps of the HPTE-treated samples' normal cross-section, annealed at 230 °C (a), 280 °C (b), and 330 °C (c), near the mid-radius. Following annealing for 1 h at 230 °C, a mean grain size of the Al matrix is 0.57 ± 0.24 μm (Fig. S1(a)), with a HAGB fraction of 73 % (Fig. S2(a)). Raising the annealing temperature to 280 °C for 1 h brings about a slight increase of the grain size to 0.91 ± 0.39 μm (Fig. S1(b)), while the fraction of HAGBs remains at 73 % (Fig. S2(b)). Further raising the annealing temperature to 330 °C for 1 h brings about a grain size increase to 1.07 ± 0.46 μm (Fig. S1(c)), and the fraction of HAGBs decreases to 71 % (Fig. S2(c)). These findings suggest that the HPTE-treated sample demonstrates a strong thermal stability within the above mentioned temperatures, in a good agreement with microhardness measurements (Fig. 3(a)). Fig. 9(d) shows the ACOM TEM orientation map for the HPTE-treated sample after annealing at 280 °C, taken near the edge where the equivalent strain is 10.5. The mean grain size in this region is 0.67 ± 0.32 μm (Fig. S1(d)), with a HAGB fraction of 73 % (Fig. S2(d)).

As the annealing temperature rose to 330 °C, the grain size of the HPTE-treated Al-2.5 Fe alloy varied between 0.57 μm and 1.07 μm near

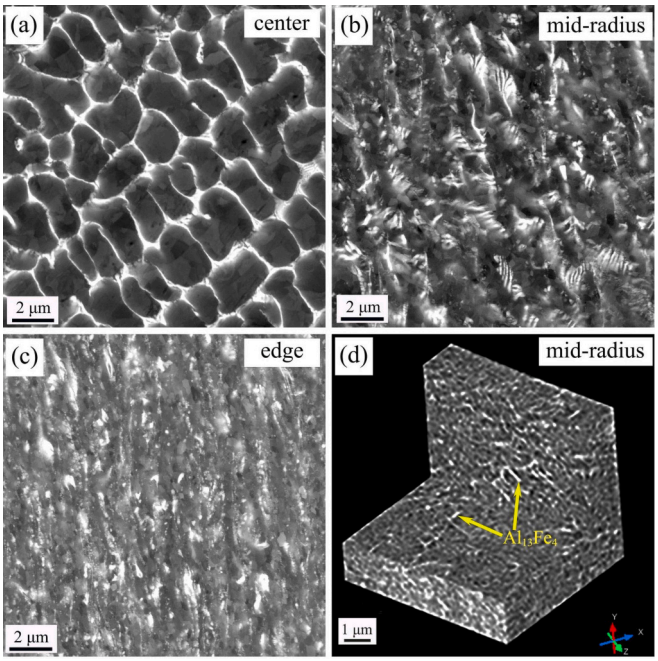

Fig. 6. Microstructure of the HPTE-treated Al—Fe alloy at three distinct positions along the normal rod cross-section (a, b, c) and NanoCT image of the HPTE-treated Al—Fe alloy at the radius midpoint (d). In all images, $Al_{13}Fe_4$ phase appears bright.

the mid-radius. However, the HAGB fraction decreased from 79 % to 71 %, contrary to the expected increase typically observed during recrystallization. Similar phenomena were reported in prior research on SPD-processed and annealed materials [33–36], which attribute this behavior to the movement of triple junctions that eliminate HAGBs and form segments of low-angle grain boundaries (LAGBs) [33].

Fig. 10(a-d) presents STEM-EDX representations of the microstructure of HPTE-treated samples, annealed at 230 °C and 280 °C, taken from edge positions along the rod's normal cross-section, where the equivalent strain is 10.5. After annealing at 230 °C for 1 h (Fig. 10(a-b)), the nanoparticles within the grains continue to effectively pin the dislocations. With the annealing temperature raised to 280 °C for 1 h (Fig. 10(c-d)), the dislocations within the grains have largely disappeared.

3.3. XRD profile analysis

The X-ray diffraction pattern of the as-cast alloy exhibits the diffraction peaks aligning with to the $Al_{13}Fe_4$ and Al phases (Fig. 11(a)). According to the XRD results (PDF data), the lattice parameters of the phases are as follows: The Al matrix (Fm3m) has $a = b = c = 0.4049$ nm, with $\alpha = \beta = \gamma = 90°$. The $Al_{13}Fe_4$ phase (R3m) has $a = b = 1.4207$ nm, $c = 0.7547$ nm, with $\alpha = \beta = 90°$ and $\gamma = 120°$. The XRD peaks for Al exhibit remarkable broadening due to HPTE processing, as shown by the (111) peak in Fig. 11(b), indicating a refinement of the Al matrix due to substantial deformation (Fig. 11(b)). Table 2 shows the XRD analysis results for the alloy following HPTE and then annealing. No significant changes are observed in lattice parameters across the whole samples, indicating that Fe atoms do not noticeably transfer into or out of the Al matrix during HPTE and annealing. The dislocation density in the HPTE-treated sample is relatively high and remains at a similar level after annealing at 230 °C. However, as the annealing temperature rises, the dislocation density decreases (Table 2). These XRD findings are consistent with the microstructural observations made via TEM.

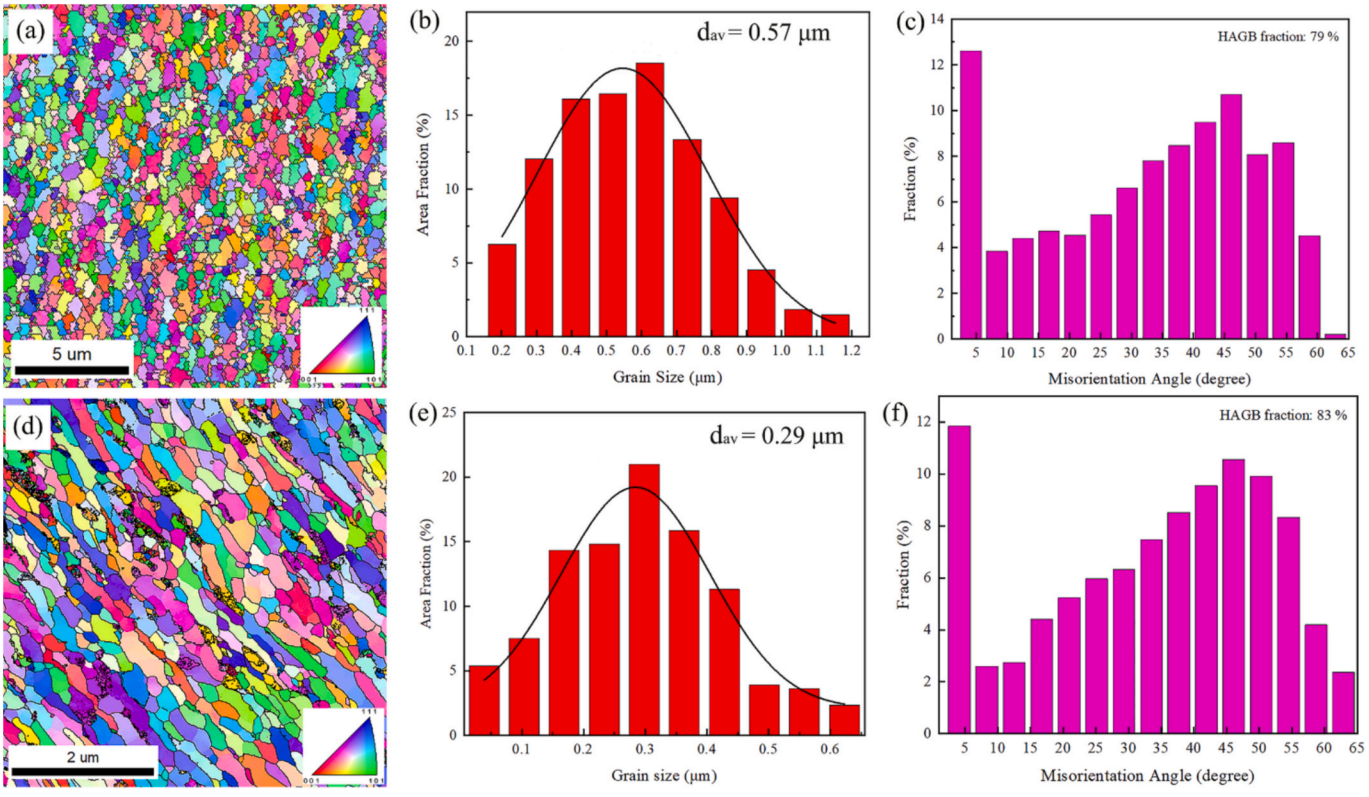

Fig. 7. (a) EBSD orientation map of the microstructure in the HPTE-treated Al—Fe alloy near the mid-radius, (b) grain size distribution, and (c) grain boundary (GB) misorientation angles. (d) ACOM orientation map of the microstructure near the sample edge, (e) grain size distribution, and (f) GB misorientation angles.

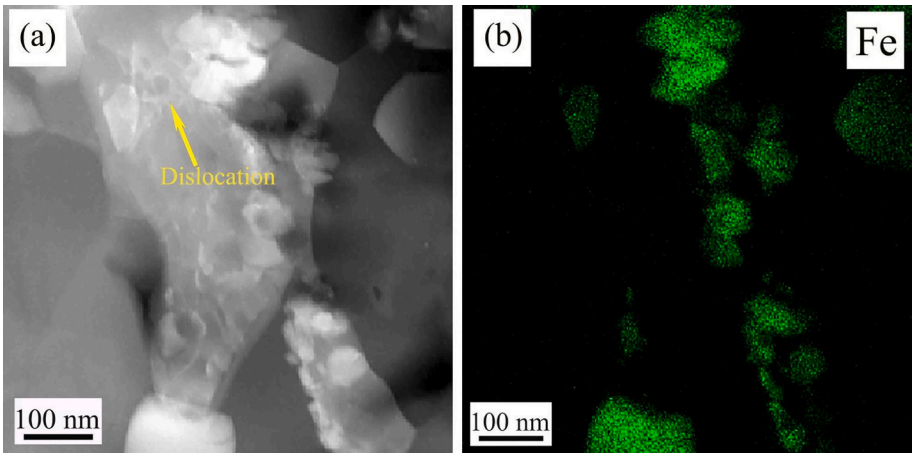

Fig. 8. (a) STEM representation of the microstructure in the HPTE-treated Al—Fe alloy, and (b) EDX map of the HPTE-treated Al—Fe alloy.

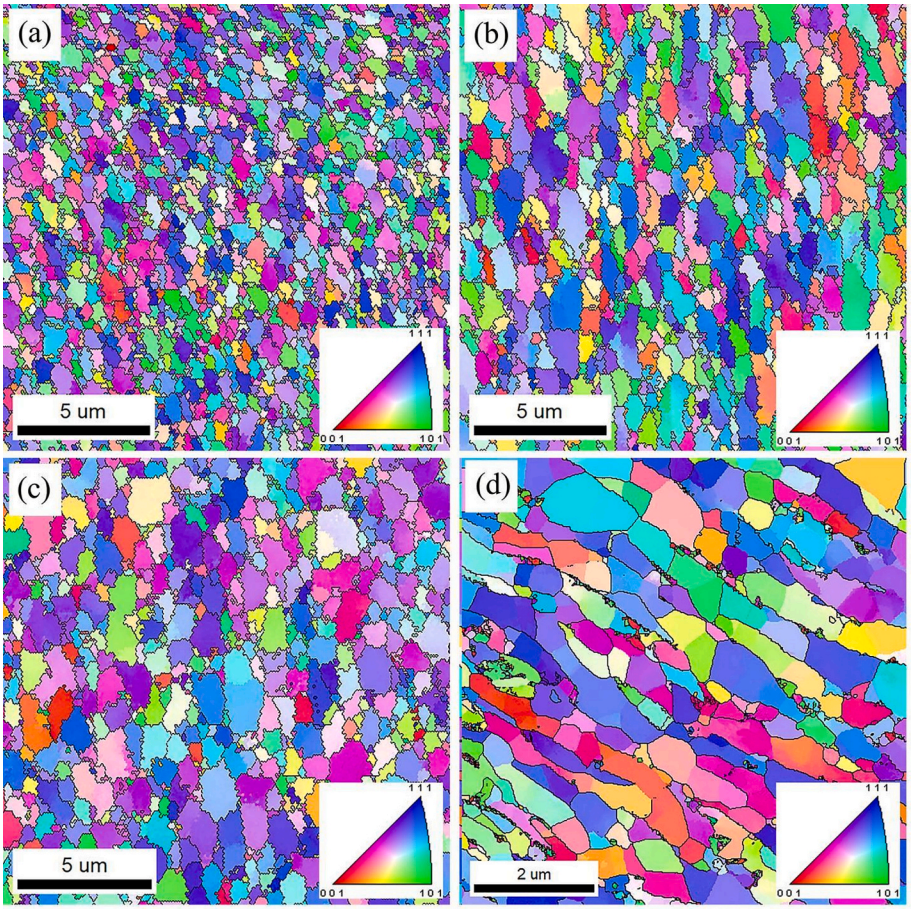

Fig. 9. Orientation maps of the Al-2.5 Fe alloy microstructure after HPTE and annealed at 230 °C (a), 280 °C (b, d), and 330 °C (c). (a, b, c) are EBSD orientation maps near the mid-radius, while (d) is the ACOM TEM orientation map near the sample edge after HPTE and annealed at 280 °C.

4. Discussion

This study demonstrates that the conventional trade-off between strength and EC in Al-2.5 Fe alloy rods can be overcome through phase refinement achieved by HPTE processing. After HPTE deformation, the Al-2.5 Fe alloy rods improve remarkably in yield strength and EC in marked contrast with their as-cast state (Fig. 3). Following annealing at 230 °C for 1 h, the HPTE-treated Al-2.5 Fe alloy retains its mechanical strength, owing to the pinning effect of micrometer- and nanometer-sized particles on dislocations and GBs (Fig. 10). The notable rise in strength is due to the refined Al-matrix grain size (Fig. 7(a-d)), a rise in dislocation density (Table 3), and the continuous $Al_{13}Fe_4$ phase network transformed into micrometer- and nanometer-sized particles (Fig. 6(b-d)) by virtue of the HPTE processing.

With respect to electrical conductivity, severe deformation reduces grain size and increases the density of structural defects, which in turn increases electron scattering and reduces conductivity. However, the fragmentation of the continuous $Al_{13}Fe_4$ network into micrometer- and

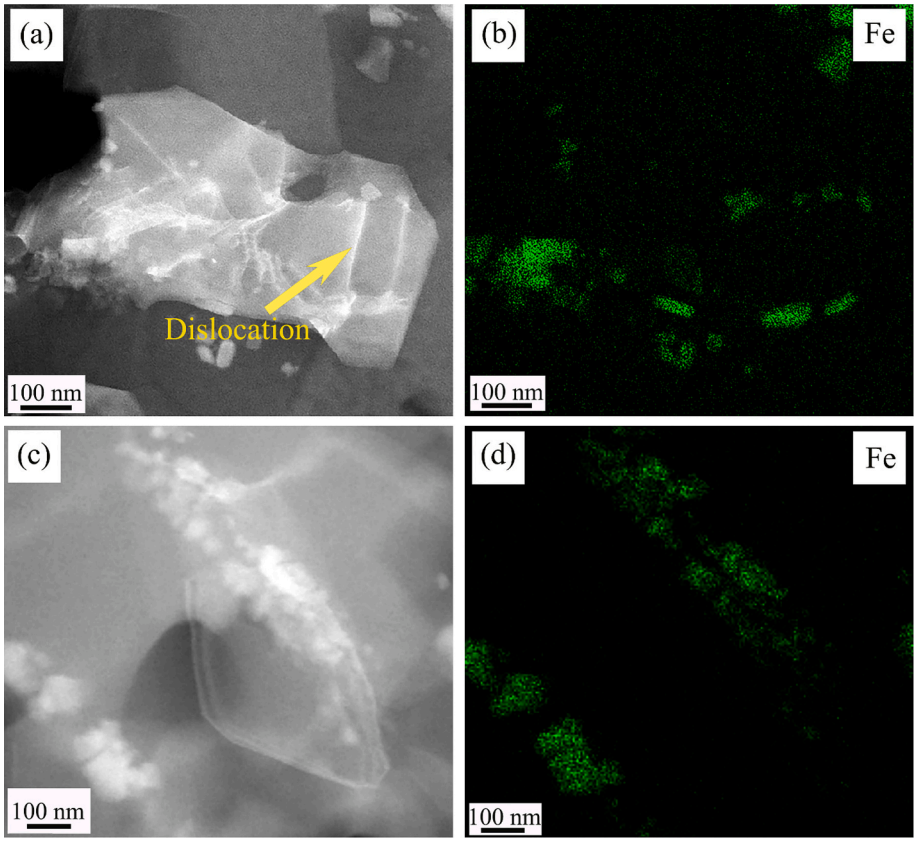

Fig. 10. STEM-EDX representations of the microstructure in HPTE-treated and annealed Al-2.5 Fe alloy specimens: annealed at 230 °C (a-b) and at 280 °C (c-d).

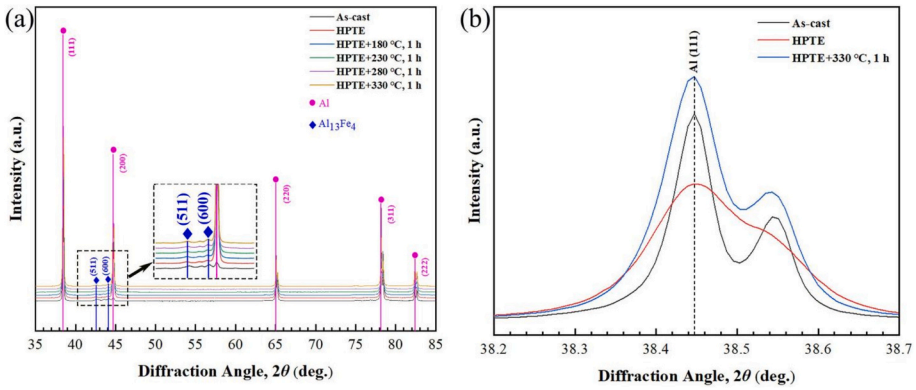

Fig. 11. The as-cast, HPTE-treated, and annealed specimens' XRD modes (a), with a magnified view of the Al (111) peak.

Table 2
Microstructure of Al-2.5 Fe alloys following HPTE at room temperature and then annealing. MR refers to the mid-radius, d_{av} represents the area-weighted average grain size, and HAGBs denote high-angle grain boundaries.

Sample	MR-d_{av} (μm) (EBSD)	Fraction of HAGBs	Edge-d_{av} (μm) (ACOM)	Fraction of HAGBs
HPTE	0.57 ± 0.22	79	0.29 ± 0.14	83
HPTE+annealing 230 °C, 1 h	0.57 ± 0.24	73	–	–
HPTE+annealing 280 °C, 1 h	0.91 ± 0.39	73	0.67 ± 0.32	73
HPTE+annealing 330 °C, 1 h	1.07 ± 0.46	71	–	–

nanometer-sized particles improves the connectivity within the Al matrix. Notably, the Al matrix has a resistivity of 2.6 μΩ·cm [37], which is much lower than an average resistivity of the $Al_{13}Fe_4$ phase at 311 μΩ·cm [38]. Consequently, the EC of the as-cast Al-2.5 Fe alloy is improved following HPTE processing. The detailed relationships between microstructure, strength, electrical conductivity, and thermal stability will be discussed in the following sections.

4.1. Strengthening mechanism

Based on microstructural explorations and XRD analysis (Section 3), the mechanisms contributing to the strength of the HPTE-treated Al-2.5 Fe alloys involve grain boundary strengthening, dislocation strengthening, and the reinforcement provided by nanoscale intermetallic particles. The input of these factors to the mechanical strength of the HPTE-

Table 3
XRD data of Al-2.5 Fe alloys following HPTE at room temperature and then annealing. "a" represents the lattice parameter, D represents the coherent scattering domain size (CSDS), $<\varepsilon^2>^{1/2}$ refers to the lattice microstrain, and ρ denotes the dislocation density.

Sample	a, (Å)	D, (nm) (XRD)	$<\varepsilon^2>^{1/2}$, (%)	$\rho_{\perp}$, (m^{-2})
As-cast	4.0492 ± 0.0002	158 ± 43	0.050 ± 0.002	3.8×10^{13}
HPTE	4.0490 ± 0.0001	84 ± 30	0.153 ± 0.003	2.2×10^{14}
HPTE+annealing 180 °C, 1 h	4.0489 ± 0.0001	103 ± 62	0.120 ± 0.004	1.4×10^{14}
HPTE+annealing 230 °C, 1 h	4.0491 ± 0.0001	98 ± 49	0.114 ± 0.004	1.4×10^{14}
HPTE+annealing 280 °C, 1 h	4.0492 ± 0.0001	134 ± 63	0.056 ± 0.005	5.1×10^{13}
HPTE+annealing 330 °C, 1 h	4.0492 ± 0.0001	151 ± 72	0.054 ± 0.005	4.3×10^{13}

treated Al-2.5 Fe alloys can be quantified as follows:

$$\sigma_{y\ 0.2} = \sigma_0 + \sigma_{GB} + \sigma_{Dis} + \sigma_{Part} \quad (3)$$

here, $\sigma_{y0.2}$ denotes the calculated yield strength, σ_0 denotes the Peierls-Nabarro stress [39], σ_{GB}, σ_{Dis}, and σ_{Part} denotes the intensified effects contributed by GBs, misorientations, and nanometer-sized intermetallic particles within the Al matrix, separately.

The input of grain boundary strengthening is given by the Hall-Petch equation [17]:

$$\sigma_{GB} = \frac{k}{\sqrt{d_{av}}} \quad (4)$$

here, k (0.04 MPa·m^{-2}) indicates the Hall-Petch coefficient for aluminum [5,40], and d_{av} represents the average grain size, determined from EBSD and ACOM orientation maps. The grain size values for the HPTE-treated and HPTE-treated and subsequently annealed at 280 °C Al-2.5 Fe alloy samples are provided in Table 2. In the HPTE-treated sample and the annealed sample, the grain size decreases progressively along the sample radius. Consequently, the grain boundary strengthening contribution in the HPTE-treated sample ranges from 53 to 74 MPa, while in the 280 °C annealed sample, it varies from 42 to 49 MPa.

The contribution from dislocations can be estimated using the Bailey-Hirsch equation [41]:

$$\sigma_{Dis} = M^*\alpha^*G^*b^*\sqrt{\rho_{\perp}} \quad (5)$$

here, M represents the Taylor factor (3.06) [36], α represents a dimensionless constant (0.33) regarding misorientation interactions [41], G represents the shear modulus of aluminum (26 GPa) [42], b represents the Burgers vector (0.286 nm for Al) [42], and $\rho_{\perp}$ represents the dislocation density, determined by XRD outcomes (Table 3).

The strengthening provided by nanometer-sized intermetallic particles occurs because these particles are obstacles for dislocation glide. Previously it had been demonstrated that dislocations can overcome these particles through two mechanisms: cutting and bypassing. If the radius of particles exceeds 2 nm, dislocations will bypass the particles in the Al matrix [43]. The hardening effect of nanometer-sized intermetallic particles is capable of being figured out through the formula according to the Orowan mechanism [6,44]:

$$\sigma_{Part} = 0.7^*M^*G^*b^*\frac{\sqrt{f_v}}{r} \quad (6)$$

here, M, G and b are the same as in Eq. (5), while f_v represents the volume fraction and r indicates the mean radius of nanoscale intermetallic particles.

Through the ImageJ software and some STEM-EDX representations, the mean radius and volume fraction of nanoscale intermetallic particles were measured. For this analysis, just nanometer-sized particles located inside of the Al matrix grains were included. The volume fraction (f_v) was determined to be 3.0 ± 0.2 % for the as-HPTE sample as well as 2.8 ± 0.2 % for the annealed HPTE-treated sample. Significantly, a slight difference in volume fraction between the two states is within the statistical error and thus holds no physical significance. In as-HPTE and annealed HPTE-treated samples, the nanoscale intermetallic particles had an average radius of 33 ± 12 nm.

Table 4 shows the calculated contributions of diverse intensified mechanisms to the mechanical strength for HPTE-treated and annealed at 280 °C samples. It is evident that dislocation strengthening contributes most to the mechanical strength in the HPTE-treated Al—Fe alloy. Following annealing at 280 °C for 1 h, the contribution from grain boundary strengthening decreases on account of grain size increase, and a similar trend is observed for misorientation strengthening. Orowan strengthening is an important player in the whole strengthening of the HPTE-treated and annealed Al—Fe alloy at 280 °C. The estimated total yield strength, based on Eqs. (3)–(6), corresponds well to the mechanical strength measured experimentally.

4.2. Tensile behavior of the UFG Al-2.5 Fe alloy

From Fig. 3(b), it is evident that the HPTE process significantly influences the tensile stress-strain behavior of the Al-2.5Fe alloy. After HPTE, the uniform elongation of the as-cast Al-2.5Fe alloy decreases notably, which can be attributed to the onset of plastic instability conditions commonly observed in ultrafine-grained materials [32,45]. According to Liu et al. [46], the distribution of uniform elongation in FCC metals can be categorized into three stages based on grain size: the low elongation stage (< ~1 μm), the nearly constant elongation stage (~1 to ~200 μm), and the decreased elongation stage with large scatter (> ~200 μm). After HPTE, the Al matrix grain size is refined to 0.29–0.57 μm, placing it within the low elongation stage, thereby leading to a reduction in uniform elongation. On the other hand, despite the decline in uniform elongation, the total elongation remains nearly unchanged after HPTE. These samples exhibit significant post-necking deformation, a characteristic behavior commonly observed in SPD materials [47–49]. While this phenomenon is intriguing from a fundamental materials science perspective, to the best of our knowledge, it has not been extensively studied in detail. This may be due to its limited relevance to practical applications. We acknowledge its scientific interest but consider it beyond the scope of the present study. However, we plan to further investigate this aspect in future research.

4.3. Electrical conductivity

A schematic summary of the microstructural observations of the Al-2.5 Fe alloy after casting and HPTE processing is presented in Fig. 12. The as-cast Al-2.5 Fe alloy features an Al matrix embedded with a continuous network of the $Al_{13}Fe_4$ phase (Fig. 12(a)). The conductive electrons scatter at lattice defects within the Al matrix, like grain boundaries, solute atoms, and vacancies, as well as on the $Al_{13}Fe_4$ phase

Table 4
Strengthening contributions from different mechanisms in HPTE-treated and annealed Al-2.5 Fe alloy (280 °C), calculated using Eqs. (3)–(6), compared to the mechanical strength measured experimentally.

Sample	σ_0 (MPa)	σ_{GB} (MPa)	σ_{Dis} (MPa)	σ_{Part} (MPa)	$\sigma_{y_{0.2}}$ (MPa)	σ_{exp} (MPa)
HPTE	10	53–74	101	86	250–271	268 ± 5
HPTE+annealing 280 °C, 1 h	10	42–49	49	84	185–192	190 ± 3

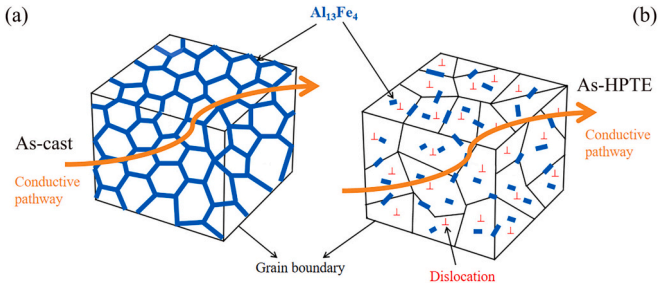

Fig. 12. Illustration of changes in evolution of the Al—Fe alloy microstructure: (a) as-cast; (b) after HPTE processing.

in as-cast Al-2.5 Fe alloy. The most significant obstacle to electron flow is the continuous $Al_{13}Fe_4$ phase network, which has a resistivity two orders of magnitude exceeding that of aluminum [37,38]. After HPTE processing, the $Al_{13}Fe_4$ phase is fragmented, the grain size is reduced, and dislocations are introduced within the grain interiors (Fig. 12(b)). The continuous $Al_{13}Fe_4$ network is broken into micrometer- and nanometer-sized particles, improving the connectivity within the Al matrix. Consequently, the scattering frequency of conduction electrons at the $Al_{13}Fe_4$ phase decreases.

The effect of diverse microstructural characteristics on ER is capable of being assessed quantitatively through Matthiessen's rule [50]:

$$\rho_{cal} = \rho_{pure} + \rho_{GB} + \rho_{Al_{13}Fe_4} + \rho_{Dis} + \rho_{vac} + \rho_{ss} \quad (7)$$

where, ρ_{pure} reaches 2.7 μΩ.cm [30], with ρ_{GB}, $\rho_{Al_{13}Fe_4}$, ρ_{Dis}, ρ_{vac}, and ρ_{ss} being the ER contributions from GBs, $Al_{13}Fe_4$ phase, and dislocations, vacancies, solute atoms, separately.

Due to grain boundaries, ER can be calculated below [51]:

$$\rho_{GB} = (3/d_{av})*\Delta\rho^{GB} \quad (8)$$

here, d_{av} is an average grain size of the Al matrix and $\Delta\rho^{GB}$ indicates the resistivity each unit density of grain boundaries reaching 2.6×10^{-16} Ωm^2 for Al [51,52]. Since the mean grain size of the as-cast sample becomes large over 300 μm, the effect of GBs on the resistivity of the as-cast alloy can be considered negligible.

The Al matrix of the as-cast sample contains a continuous network of the $Al_{13}Fe_4$ phase (Fig. 12(a)), which represents an obstacle for the scattering electrons path. We can assume that the effect of the $Al_{13}Fe_4$ phase on the ER is similar to that of grain boundaries and can be calculated using the equation, similar to Eq. (8):

$$\rho_{Al_{13}Fe_4} = (3/L_{av})*\Delta\rho^{Al_{13}Fe_4} \quad (9)$$

where $L_{av} = 4.5 \pm 2$ μm is an average distance between the walls of the closed cell of the $Al_{13}Fe_4$ phase network and $\Delta\rho^{Al_{13}Fe_4}$ is the resistivity of $Al_{13}Fe_4$ phase which is 311×10^{-16} Ωm^2 [38]. The contribution of the $Al_{13}Fe_4$ phase to the resistivity of the as-cast sample is estimated as 2.7 μΩ.cm.

The contributions from dislocations, vacancies, and solute atoms to the resistivity of the as-cast Al—Fe alloy are negligibly small on account of a low density of dislocations/vacancies and zero solid state solubility of Fe in Al and can be ignored. Therefore, the calculated electrical resistance of as-cast Al—Fe alloy is 4.77 μΩ.cm or 36.5 % IACS, which is very close to the measured values of 37.3 % IACS, which indicates that our approach to calculating the contribution of a continuous network of intermetallic $Al_{13}Fe_4$ phase is correct.

After HPTE processing, the $Al_{13}Fe_4$ phase was fragmented into micron- and nanometer-sized particles, the mean AL-matrix grain size was reduced, and dislocation density increased. However, the EC of the HPTE-treated alloy exceeds that of the as-cast alloy. Most likely this correlates with the fragmentation of the continuous network of the intermetallic $Al_{13}Fe_4$ phase. Indeed, the input of grain boundaries to resistivity, determined by Eq. (8), for the HPTE-treated sample is between 0.14 and 0.27 μΩ.cm, and for the sample annealed at 280 °C is between 0.09 and 0.12 μΩ.cm.

The inpu of dislocation density to the ER is even smaller than that from grain boundaries. It can be calculated as [51,52]:

$$\rho_{Dis} = \rho_{\perp}*\Delta\rho^{Dis} \quad (10)$$

here, $\rho_{\perp}$ indicates the dislocation density and $\Delta\rho^{Dis}$ reaches 2.7×10^{-25} Ωm^3 [51,52]. Using the values obtained from the XRD results (Table 2), the input of dislocation to ER is calculated to be 0.006 μΩ·cm after HPTE and 0.004 μΩ·cm following subsequent annealing, both of which are considered negligible.

The effect of vacancies on the ER of the HPTE-treated sample is able to be determined using the following equation [51–53]:

$$\rho_{vac} = N_{vac}*\Delta\rho^{Vac} \quad (11)$$

where N_{vac}represents vacancy concentration and $\Delta\rho^{Vac}$ reaches 190 μΩ.cm each vacancy for Al [54]. Given that the vacancy concentration in metals following HPT processing commonly ranges between 10^{-4} and 10^{-3} (in atomic fraction) [52,55], the maximal vacancy contribution to ER is about 0.2 μΩ.cm. We should note that this is an overestimated value because vacancy concentration in Ref. [52, 55] was obtained for Al deformed by High Pressure Torsion with significantly higher strain than that at HPTE in the present work.

These estimates indicate that microstructural defects have a relatively minor impact on the EC of the material, even after acute plastic deformation in the as-cast Al-2.5 Fe. However, the breakdown of the continuous intermetallic phase network improves connectivity in the Al matrix, facilitating a longer free path for conductive electrons. According to the experimentally measured electrical conductivity, this improvement results in an increase of at least 5–7 % IACS in as-cast Al-2.5 Fe.

4.4. Thermal stability

Following 1 h of annealing below 230 °C, the microhardness, average grain size, and dislocation density of HPTE-treated Al-2.5 Fe alloy rods remained virtually unchanged. Consequently, the HPTE-treated Al-2.5 Fe alloy demonstrates better thermal stability than many other Al alloys subjected to severe plastic deformation [56]. This improved stability results from the exceptional thermal stability of the $Al_{13}Fe_4$ intermetallic phase [12] as well as the strengthening effect of micrometer- and nanometer-sized $Al_{13}Fe_4$ particles, which inhibit Al grain boundary transfer, thus preventing dislocation recovery and grain coarsening, and maintaining the UFG constitution. The microhardness of HPTE-treated Al-2.5 Fe alloy rods decreases to approximately 72 HV after an in-depth rise in the temperature increasing to 330 °C for 1 h, which is still higher than that of the as-cast state.

5. Conclusions

An immiscible Al-2.5 Fe alloy was processed through HPTE and subsequently annealed at various temperatures. This treatment was shown to simultaneously enhance both the yield strength and electrical conductivity (EC) of the as-cast Al-2.5 Fe alloy. Additionally, the ultrafine-grained HPTE-treated alloy demonstrated excellent thermal stability. The related conclusions can be reached:

1. HPTE processing drives to form a gradient ultrafine-grained microstructure in the Al-2.5 Fe alloy at RT.
2. HPTE significantly increases the mechanical strength from 110 MPa to 268 MPa, primarily due to the refined Al matrix grain size to the sub-micrometer range, an elevated density of dislocations, and the fragmentation of the $Al_{13}Fe_4$ phase into nanometer-sized particles.

3. HPTE enhances the EC between 37.3 % IACS and 44.7 % IACS by breaking the continuous $Al_{13}Fe_4$ network into micrometer- and nanometer-sized particles, improving the connectivity within the Al matrix.
4. The ultrafine-grained HPTE-treated Al-2.5 Fe alloy demonstrates high thermal stability, attributed to micrometer- and nanometer-sized particles intensifying GBs and dislocations.
5. The shape, dimensions, and spatial distribution of the $Al_{13}Fe_4$ phase are crucial players in measuring the thermal stability, EC, and mechanical performances of the Al-2.5 Fe alloy.

CRediT authorship contribution statement

Rui Xu: Writing – original draft, Methodology, Investigation. **Yemao Lu:** Writing – review & editing, Methodology, Investigation, Conceptualization. **Yuting Dai:** Writing – review & editing, Methodology, Investigation. **Rafaela Debastiani:** Writing – review & editing, Investigation. **Horst Hahn:** Writing – review & editing, Supervision. **Yulia Ivanisenko:** Writing – review & editing, Supervision, Conceptualization.

Declaration of competing interest

The authors declare that they have no known competing financial interests or personal relationships that could have appeared to influence the work reported in this paper.

Acknowledgements

This work was partially supported by China Scholarship Council [grant no. 202006670001]. The authors gratefully acknowledge Karlsruhe Nano Micro Facility (KNMFi, www.knmf.kit.edu), a Helmholtz Research Infrastructure at Karlsruhe Institute of Technology (KIT, www.kit.edu), for providing advanced characterization techniques. This work was partly carried out with the support of the Joint Laboratory Model and Data-driven Materials Characterization (JL MDMC), a cross-center platform of the Helmholtz Association. The Xradia 810 Ultra (nanoCT) core facility was supported (in part) by the 3DMM2O– Cluster of Excellence (EXC-2082/1390761711). R.D. acknowledge the support by the Cluster of Excellence 3DMM2O (EXC_2082/1-236 390761711) funded by the German Research Foundation (DFG). We are gratefully indebted to Dr. R. Kruk for valuable discussions and Dr. M. Murashkin for valuable discussion of the results.

Appendix A. Supplementary data

Supplementary data to this article can be found online at https://doi.org/10.1016/j.matchar.2025.114956.

Data availability

Data will be made available on request.

References

[1] K.A. Trowell, S. Goroshin, D.L. Frost, J.M. Bergthorson, Aluminum and its role as a recyclable, sustainable carrier of renewable energy, Appl. Energy 275 (2020) 115112.
[2] X. Sauvage, E.V. Bobruk, M.Yu. Murashkin, Y. Nasedkina, N.A. Enikeev, R. Z. Valiev, Optimization of electrical conductivity and strength combination by structure design at the nanoscale in Al–Mg–Si alloys, Acta Mater. 98 (2015) 355–366.
[3] F. Kiessling, P. Nefzger, J.F. Nolasco, U. Kaintzyk, Overhead Power Lines: Planning, Design, Construction, Springer, 2014.
[4] S.N. Khangholi, M. Javidani, A. Maltais, X.G. Chen, Effects of natural aging and pre-aging on the strength and electrical conductivity in Al-Mg-Si AA6201 conductor alloys, Mater. Sci. Eng. A 820 (2021) 141538.
[5] M.Y. Murashkin, I. Sabirov, A.E. Medvedev, N.A. Enikeev, W. Lefebvre, R.Z. Valiev, X. Sauvage, Mechanical and electrical properties of an ultrafine grained Al–8.5 wt. % RE (RE= 5.4 wt.% Ce, 3.1 wt.% La) alloy processed by severe plastic deformation, Mater. Des. 90 (2016) 433–442.
[6] A. Mohammadi, N.A. Enikeev, M.Y. Murashkin, M. Arita, K. Edalati, Developing age-hardenable Al-Zr alloy by ultra-severe plastic deformation: significance of supersaturation, segregation and precipitation on hardening and electrical conductivity, Acta Mater. 203 (2021) 116503.
[7] A. Duchaussoy, X. Sauvage, K. Edalati, Z. Horita, G. Renou, A. Deschamps, F. De Geuser, Structure and mechanical behavior of ultrafine-grained aluminum-iron alloy stabilized by nanoscaled intermetallic particles, Acta Mater. 167 (2019) 89–102.
[8] S.O. Rogachev, E.A. Naumova, E.S. Vasileva, R. Sundeev, Al–Ca, Al–Ce, and Al–La eutectic aluminum alloys processed by high-pressure torsion, Adv. Eng. Mater. 24 (2) (2022) 2100772.
[9] A.E. Medvedev, M.Y. Murashkin, N.A. Enikeev, I. Bikmukhametov, R.Z. Valiev, P. D. Hodgson, R. Lapovok, Effect of the eutectic Al-(Ce, La) phase morphology on microstructure, mechanical properties, electrical conductivity and heat resistance of Al-4.5 (Ce, La) alloy after SPD and subsequent annealing, J. Alloys Compd. 796 (2019) 321–330.
[10] A.E. Medvedev, M.Y. Murashkin, N.A. Enikeev, R.Z. Valiev, P.D. Hodgson, R. Lapovok, Enhancement of mechanical and electrical properties of Al-RE alloys by optimizing rare-earth concentration and thermo-mechanical treatment, J. Alloys Compd. 745 (2018) 696–704.
[11] M. Wang, J. Wu, S. Yang, M. Knezevic, Z. Huang, Y. Zhao, J. Wang, et al., Processing of an as-cast Al-7.5 wt% Y eutectic alloy by rolling and annealing to improve the tradeoff between strength and electrical conductivity, Mater. Sci. Eng. A 890 (2024) 145950.
[12] A. Sharma, Y. Morisada, K. Ushioda, H. Fujii, Elucidation on the correlation between thermal stability of $Al_{13}Fe_4$ intermetallic phase and mechanical properties of the Al-Fe alloy fabricated via friction stir alloying, J. Alloys Compd. 967 (2023) 171732.
[13] Z.M. Shi, K. Gao, Y.T. Shi, Y. Wang, Microstructure and mechanical properties of rare-earth-modified Al-1Fe binary alloys, Mater. Sci. Eng. A 632 (2015) 62–71.
[14] B.N. Kim, T. Kishi, Finite element simulation of Zener pinning behavior, Acta Mater. 47 (7) (1999) 2293–2301.
[15] J.M. Cubero-Sesin, Z. Horita, Age hardening in ultrafine-grained Al-2 pct Fe alloy processed by high-pressure torsion, Metall. Mater. Trans. A 46 (2015) 2614–2624.
[16] K. Edalati, A. Bachmaier, V.A. Beloshenko, Y. Beygelzimer, V.D. Blank, W.J. Botta, X. Zhu, et al., Nanomaterials by severe plastic deformation: review of historical developments and recent advances, Mater. Res. Lett. 10 (4) (2022) 163–256.
[17] C.S. Pande, K.P. Cooper, Nanomechanics of Hall–Petch relationship in nanocrystalline materials, Prog. Mater. Sci. 54 (6) (2009) 689–706.
[18] Y. Estrin, A. Vinogradov, Extreme grain refinement by severe plastic deformation: a wealth of challenging science, Acta Mater. 61 (3) (2013) 782–817.
[19] Y. Ivanisenko, R. Kulagin, V. Fedorov, A. Mazilkin, T. Scherer, B. Baretzky, H. Hahn, High pressure torsion extrusion as a new severe plastic deformation process, Mater. Sci. Eng. A 664 (2016) 247–256.
[20] R. Kulagin, Y. Beygelzimer, Y. Estrin, Y. Ivanisenko, B. Baretzky, H. Hahn, A mathematical model of deformation under high pressure torsion extrusion, Metals 9 (3) (2019) 306.
[21] B. Omranpour, Y. Ivanisenko, R. Kulagin, L. Kommel, E.G. Sanchez, D. Nugmanov, J. Gubicza, et al., Evolution of microstructure and hardness in aluminum processed by high pressure torsion extrusion, Mater. Sci. Eng. A 762 (2019) 138074.
[22] D. Nugmanov, A. Mazilkin, H. Hahn, Y. Ivanisenko, Structure and tensile strength of pure Cu after high pressure torsion extrusion, Metals 9 (10) (2019) 1081.
[23] R. Xu, Y. Lu, Y. Dai, A. Brognara, H. Hahn, Y. Ivanisenko, Processing of high-strength thermal-resistant Al-2.2% cerium-1.3% lanthanum alloy rods with high electric conductivity by high pressure torsion extrusion, J. Mater. Sci. (2024) 1–16.
[24] J. Hu, R. Kulagin, Y. Ivanisenko, B. Baretzky, H. Zhang, Finite element modeling of conform-HPTE process for a continuous severe plastic deformation path, J. Manuf. Process. 55 (2020) 373–380.
[25] Object Research Systems (ORS) Inc, Dragonfly: 3D Visualization and Analysis Solutions for Scientific and Industrial Data. http://www.theobjects.com/dragonfly/, 2022.
[26] M. Baig, H.R. Ammar, A.H. Seikh, Thermo-mechanical responses of nanocrystalline Al-Fe alloy processed using mechanical alloying and high frequency heat induction sintering, Mater. Sci. Eng. A 655 (2016) 132–141.
[27] Vahid Tavakkoli, Evgeniy Boltynjuk, Torsten Scherer, Andrey Mazilkin, Yulia Ivanisenko, Tamas Ungar, Christian Kübel, Precipitate-mediated enhancement of mechanical and electrical properties in HPTE-processed Al–Mg–Si alloy, Mater. Sci. Eng. A 906 (2024) 146556, https://doi.org/10.1016/j.msea.2024.146556. ISSN 0921-5093.
[28] P.J. Apps, J.R. Bowen, P.B. Prangnell, The effect of coarse second-phase particles on the rate of grain refinement during severe deformation processing, Acta Mater. 51 (10) (2003) 2811–2822.
[29] R. Pippan, F. Wetscher, M. Hafok, The limits of refinement by severe plastic deformation, Adv. Eng. Mater. 8 (11) (2006) 1046–1056.
[30] F.J. Humphreys, P.N. Kalu, The plasticity of particle-containing polycrystals, Acta Metall. Mater. 38 (6) (1990) 917–930.
[31] F.J. Humphreys, M. Hatherly, Recrystallization and Related Annealing Phenomena, Elsevier, 2012.
[32] H.W. Kim, S.B. Kang, N. Tsuji, Y. Minamino, Elongation increase in ultra-fine grained Al-Fe-Si alloy sheets, Acta Mater. 53 (6) (2005) 1737–1749.
[33] A. Godfrey, O.V. Mishin, Controlled annealing of sandwich-structured aluminum AA1050 for optimized combinations of strength and ductility, Mater. Sci. Eng. A 735 (2018) 228–235.

[34] O.V. Mishin, A. Godfrey, D.J. Jensen, N. Hansen, Recovery and recrystallization in commercial purity aluminum cold rolled to an ultrahigh strain, Acta Mater. 61 (14) (2013) 5354–5364.
[35] G.H. Zahid, Y. Huang, P.B. Prangnell, Microstructure and texture evolution during annealing a cryogenic-SPD processed Al-alloy with a nanoscale lamellar HAGB grain structure, Acta Mater. 57 (12) (2009) 3509–3521.
[36] X. Chen, W. Wang, H. Yang, G. Huang, D. Xia, A. Tang, F. Pan, et al., Microstructure evolution, mechanical properties and deformation characteristics of ultrafine-grained annealed pure aluminum, Mater. Sci. Eng. A 846 (2022) 143320.
[37] F.R. Fickett, Aluminum-1. A review of resistive mechanisms in aluminum, Cryogenics 11 (5) (1971) 349–367.
[38] P. Popčević, A. Smontara, J. Dolinšek, P. Gille, Anisotropic transport properties of the $Al_{13}Fe_4$ decagonal approximant, Croat. Chem. Acta 83 (1) (2010) 101–105.
[39] G.E. Totten, D.S. MacKenzie, Handbook of Aluminum, Vol. 1, Physical Metallurgy and Processes, CRC Press, Boca Raton, 2003.
[40] D.B. Witkin, E.J. Lavernia, Synthesis and mechanical behavior of nanostructured materials via cryomilling, Prog. Mater. Sci. 51 (1) (2006) 1–60.
[41] N. Hansen, X. Huang, Microstructure and flow stress of polycrystals and single crystals, Acta Mater. 46 (5) (1998) 1827–1836.
[42] K. Edalati, D. Akama, A. Nishio, S. Lee, Y. Yonenaga, J.M. Cubero-Sesin, Z. Horita, Influence of dislocation-solute atom interactions and stacking fault energy on grain size of single-phase alloys after severe plastic deformation using high-pressure torsion, Acta Mater. 69 (2014) 68–77.
[43] K.L. Kendig, D.B. Miracle, Strengthening mechanisms of an Al-Mg-Sc-Zr alloy, Acta Mater. 50 (16) (2002) 4165–4175.
[44] B.Q. Han, F.A. Mohamed, E.J. Lavernia, Tensile behavior of bulk nanostructured and ultrafine grained aluminum alloys, J. Mater. Sci. 38 (2003) 3319–3324.
[45] Y. Wang, M. Chen, F. Zhou, E. Ma, High tensile ductility in a nanostructured metal, Nature 419 (6910) (2002) 912–915.
[46] H. Liu, Y. Shen, J. Ma, P. Zheng, L. Zhang, Grain size dependence of uniform elongation in single-phase FCC/BCC metals, J. Mater. Eng. Perform. 25 (2016) 3599–3605.
[47] W. Wei, S.L. Wang, K.X. Wei, I.V. Alexandrov, Q.B. Du, J. Hu, Microstructure and tensile properties of CuAl alloys processed by ECAP and rolling at cryogenic temperature, J. Alloys Compd. 678 (2016) 506–510.
[48] X.H. An, Q.Y. Lin, S.D. Wu, Z.F. Zhang, The influence of stacking fault energy on the mechanical properties of nanostructured Cu and Cu-Al alloys processed by high-pressure torsion, Scr. Mater. 64 (10) (2011) 954–957.
[49] P. Zhang, X.H. An, Z.J. Zhang, S.D. Wu, S.X. Li, Z.F. Zhang, T.G. Langdon, et al., Optimizing strength and ductility of Cu–Zn alloys through severe plastic deformation, Scr. Mater. 67 (11) (2012) 871–874.
[50] B. Raeisinia, W.J. Poole, D.J. Lloyd, Examination of precipitation in the aluminum alloy AA6111 using electrical resistivity measurements, Mater. Sci. Eng. A 420 (1–2) (2006) 245–249.
[51] A.S. Karolik, A.A. Luhvich, Calculation of electrical resistivity produced by dislocations and grain boundaries in metals, J. Phys. Condens. Matter 6 (4) (1994) 873.
[52] Y. Miyajima, S.Y. Komatsu, M. Mitsuhara, S. Hata, H. Nakashima, N. Tsuji, Change in electrical resistivity of commercial purity aluminum severely plastic deformed, Philos. Mag. 90 (34) (2010) 4475–4488.
[53] D. Setman, E. Schafler, E. Korznikova, M.J. Zehetbauer, The presence and nature of vacancy type defects in nanometals detained by severe plastic deformation, Mater. Sci. Eng. A 493 (1–2) (2008) 116–122.
[54] A. Khellaf, A. Seeger, R.M. Emrick, Quenching studies of lattice vacancies in high-purity aluminum, Mater. Trans. 43 (2) (2002) 186–198.
[55] J. Čížek, M. Janeček, T. Vlasák, B. Smola, O. Melikhova, D. SV, The development of vacancies during severe plastic deformation, Mater. Trans. 60 (8) (2019) 1533–1542.
[56] Z. Horita, T. Fujinami, M. Nemoto, T.G. Langdon, Equal-channel angular pressing of commercial aluminum alloys: grain refinement, thermal stability and tensile properties, Metall. Mater. Trans. A 31 (2000) 691–701.